

Using a Region Growth Algorithm and Deep Reinforcement Learning for Detecting Breast Arterial Calcification in Mammograms

JINN-YI YEH^{1,*}, SHENG-YOU WU¹ AND SIWA CHAN²

¹*Department of Management Information Systems
National Chiayi University
Chiayi, 600 Taiwan*

E-mail: {jyeh; s1081073}@mail.ncyu.edu.tw

²*Department of Medical Imaging
Taichung Tzu Chi Hospital, Taiwan
E-mail: chan.siwa@gmail.com*

According to a literature review, breast arterial calcification (BAC) in mammograms can be used to predict the risk of cardiovascular disease, including coronary artery disease, atherosclerotic cardiovascular disease, and arrhythmia. This study applied a deep Q network and a state-action-reward-state-action learning algorithm combined with a deep reinforcement learning (RL) network to construct a computer-aided diagnosis system for detecting BAC in mammograms. The proposed system has an artificial agent that automatically learns the strategy and can iteratively modify the focus of attention from an initial bounding box to a smaller bounding box containing the BAC area. Then, the agent constructs a deep learning feature representation within the bounding box that is used to allow deep RL to determine the next action, such as transforming or scaling the current bounding box or triggering the end of the search process. The experimental results prove that the deep RL network with numerous training samples is significantly better than the regional growth method. The precision, recall, and F -measure of the proposed system are 0.9498, 0.9575, and 0.9536, respectively. For 50 ground truth samples, the average Intersection over Union (IoU) of the proposed system is 0.9355, minimum IoU is 0.9010, maximum IoU is 0.9591, median IoU is 0.9363, and standard deviation of the IoU is 0.0132. Thus, the proposed computer-aided diagnosis system can assist radiologists to make preliminary auxiliary judgments for detecting BAC in mammograms.

Keywords: deep reinforcement learning, convolutional neural networks, mammograms, breast artery calcification, cardiovascular diseases

1. INTRODUCTION

Deep learning is a branch of state-of-the-art machine learning in which highly abstract features are extracted from large sets of training data under mostly unsupervised situations. A computer finds it difficult to understand the meaning of original sensory input data. The input might represent the portrait of a person as a collection of pixel values. It can be difficult for a computer to identify objects from a set of pixel mappings. It seems remarkably difficult for a computer to learn or evaluate this type of mapping. Deep learning solves this problem by decomposing the complex mapping required into a series of simple mappings. Deep learning uses complex structures or multiple processing layers composed of

Received September 15, 2020; revised December 14, 2020; accepted February 25, 2021.
Communicated by Ching-Chun Huang.

* Corresponding author.

multiple nonlinear transformations to perform operations on data. Its greatest advantage is that it can use unsupervised or semisupervised methods, instead of manually obtaining features, to perform efficient learning, such as feature learning and hierarchical feature selection. Several deep learning frameworks, such as deep neural networks, convolutional neural networks (CNNs), deep belief networks, and recurrent neural networks, have achieved excellent results in computer vision, speech recognition, natural language processing, audio recognition, and bioinformatics. Deep learning has been used under various names since the 1940s. This field has been renamed many times, which reflects the disparate influences of researchers with diverse viewpoints [1].

Another advanced type of machine learning is reinforcement learning (RL), which allows the system to benefit from learning by interacting with the environment. RL is inspired by psychology. The basic idea is to learn the optimal strategy for accomplishing the goal by maximizing the cumulative reward value that the agent obtains from the environment. Therefore, RL methods are more focused on learning problem-solving strategies. With the rapid development of human society, in increasingly complex realistic scene tasks, deep learning systems must automatically learn abstract representations of large-scale input data and use these representations as a basis for self-incentivizing RL. RL has been widely used in industrial manufacturing, simulation, robot control, optimization, scheduling, games, and other fields [2].

Modeling strategies and value functions are generally required in RL. Early RL algorithms mainly considered states and actions to solve discrete and limited problems. These algorithms often used tables to record probability values. However, in many practical problems, the status and action spaces of some tasks are remarkably large. For example, the game of Go has 3^{361} to 10^{170} states, and the number of moves (*i.e.*, the position of the drop) is 361. Moreover, the status and action spaces of some tasks are continuous. For example, in autonomous driving, the environmental state sensed by the agent is described by various traditional device data. To effectively solve the aforementioned problems, a complex network function [such as a deep learning network (Fig. 1)] can be added to enable the agent to perceive more complex environmental conditions. Complex networks can establish highly complex strategies to improve RL, thereby increasing the performance of the algorithm and improving its generalization. An architecture that combines deep learning and RL is called deep RL. Systems with this architecture use RL to define problems and optimize goals as well as deep learning to manage strategies and value functions [2]. Few studies have used deep RL for medical image processing.

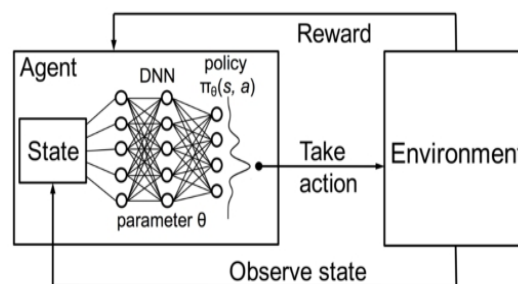


Fig. 1. Architecture of deep RL [3].

The American Cancer Society currently recommends that women receive mammograms once a year to promote the early detection of breast cancer in women over the age of 40. Those who are not routinely screened for coronary artery disease are advised to do so as soon as possible. Several prospective and cross-sectional studies in the past few years have proven that the severity of atherosclerosis and cardiovascular disease can be assessed using mammography; however, even when mammography detects breast artery calcification (BAC), the problem is often ignored [4].

Breast masses have various image features, such as image grayscale, mass acupuncture shape, smoothness, and color block size. These features can be calculated as various values through a series of algorithms, such as the grayscale co-occurrence matrix calculation. After obtaining the feature values of the image, relevant algorithms, such as stepwise feature selection and heuristic algorithms, can be used for feature filtering. When developing a series of algorithms, one might retain features with excellent classification effects to improve the efficiency of the later classification algorithms. Such retention can also avoid redundant features and affect the subsequent classification results. If one wishes to use a machine learning method with input features, screened features can be subjected to machine learning for determining the feature statistics and analyzing the features to classify different mass types, such as benign and malignant masses. The shortcomings of this method are as follows: (1) confirming whether the selected features are the best combination for tumor classification is impossible and (2) manual procedures must be used to edit out regions of interest (ROIs), because the automated tumor detection technology is not yet completely mature [5].

To solve the aforementioned problems, a deep RL model can be applied. Caicedo and Lazebnik [6] proposed a deep Q network (DQN) for effective target detection; however, their system can manage only a limited amount of information. The following obstacles must be overcome when applying the aforementioned system to medical image analysis; (1) Expanding from visual target categories (such as animals and cars) to targets in medical images (such as tumors and BAC), these are often in shape, appearance, position, background, and size have poor consistency; (2) The high dimensionality of medical images is a considerable challenge for DQN training procedures. Ghesu *et al.* [7] applied the DQN for the detection of anatomical markers. Their visual class used a consistent pattern and extracted small fixed areas from medical images. They also improved the accuracy and speed of detection. Another commonly used deep RL model is state-action-reward-state-action (SARSA) algorithm, which is used for learning Markov decision process strategies [8]. Travník *et al.* [9] proposed a reactive RL algorithm that can take immediate action after observing new state information to solve the problem of asynchronous environments. They compared the performance of the reactive SARSA learning algorithm with that of the traditional SARSA learning algorithm for two asynchronous robot tasks (emergency stop and impact prevention). The results of Travník *et al.* indicated that the reactive SARSA algorithm had a shorter reaction time than the traditional SARSA algorithm.

Through our literature review, we found that BAC in mammograms can be used to predict the risk of cardiovascular disease. In this study, we used the DQN and SARSA RL algorithms to construct a computer-aided diagnosis system that does not require input features to detect BAC in mammograms. Our agent can automatically learn strategies and describe how to iteratively modify the focus of attention from the initial large bounding box to a smaller bounding box containing the presence of BAC. Our agent constructs a

deep learning feature representation in the current bounding box, which is used to let deep RL decide the next action, such as transforming the current bounding box, scaling the current bounding box, or triggering the end of the search process.

Moreover, after our preliminary study of deep RL [16], we found that the most difficult part of the RL model is the preparation of training samples, which is remarkably time-consuming and labor-intensive. Therefore, according to the line segment characteristics of breast calcified blood vessels, this study used the region growth algorithm to segment the BAC in mammograms to provide additional BAC training samples. The remainder of this paper is organized as follows: Section 2 describes related work; Section 3 details the research methods used in this study; Section 4 presents an analysis of the experimental results; Section 5 provides the conclusions.

2. RELATED WORK

In this section, we present brief reviews of using BAI to predict heart diseases, introduction to RL, and the application of deep RL for medical image processing.

2.1 Use BAI to Predict Heart Diseases

Many studies have proven that evidence regarding BAC from mammograms can be used to predict the risk of cardiovascular disease, including coronary artery disease, atherosclerotic cardiovascular disease, and arrhythmia. For examples, Rotter *et al.* [10] established a correlation among BAC, coronary artery disease risk factors, and a history of atherosclerotic cardiovascular disease. They used BAC to predict the relative risk of atherosclerotic cardiovascular disease. The results of Rotter *et al.* indicated that among 1,919 women, 268 exhibited BAC. Moreover, five cardiovascular risk factors (age, hypertension, hypercholesterolemia, diabetes, and menopause) were observed in these women. Positive BAC also has a significantly higher incidence than atherosclerotic cardiovascular diseases, such as angina pectoris, myocardial infarction, abnormal angiography, stroke, and coronary artery bypass grafting. Logistic regression analysis indicated that BAC and atherosclerotic cardiovascular disease have a strong correlation with other atherosclerotic risk factors (including hypertension, smoking, diabetes, age, and family history). Thus, Rotter *et al.* found that BAC is highly correlated with cardiovascular morbidity and may be a practical tool used as a risk indicator for atherosclerosis in women.

Hendriks *et al.* [11] explored the relationship between BAC, cardiovascular risk factors, and cardiovascular risk through a systematic literature review and meta-analysis. They found that the occurrence of BAC is associated with an increased risk of cardiovascular disease and some known cardiovascular risk factors. The aforementioned authors also proved that unlike endometrial atherosclerosis, mid-layer arterial calcification may have an effect on cardiovascular disease. Hendriks *et al.* [12] also investigated the association of BAC with the incidences of cardiovascular disease and Type 2 diabetes. They conducted a series of case studies by using many samples and long-term tracking, which provided sufficient data for multivariate analysis. Their analysis indicated that the presence of BAC is related to cardiovascular disease. Severe BAC increases the risk of cardiovascular disease by approximately 3 times, which indicates that medial nonatherosclerosis may have an effect on cardiovascular disease.

Chadashvili *et al.* [13] investigated the use of BAC in mammograms and coronary artery calcification scores on coronary tomography scans as markers for judging the risk of developing coronary artery disease symptoms. Their study comprised 145 women with coronary artery tomography. All the mammograms were captured within a year. They scored coronary artery calcification by multiplying the calcification area by the weight value and assigning it to the highest Hounsfield Unit. Then, the aforementioned authors summed the scores of all the lesions and presented the scores obtained using the Agaston method. Their experimental results proved that the correlation score between the BAC and coronary artery calcification was greater than 11, which indicates that the possibility of the BAC predicting low-risk coronary artery diseases is higher than that of predicting medium- and high-risk coronary heart diseases. This result confirms that BAC in mammograms can be used as an index to predict the risk of coronary artery disease.

Zuin *et al.* [14] replied to the journal editor that coronary artery calcification is a crucial risk factor for coronary artery disease, and vascular calcification has been proven to increase the risk of coronary artery disease in patients with atypical coronary artery disease. Surveys have indicated that BAC is a risk factor for cardiovascular and coronary artery disease in many women. A total of 35,542 patients had participated in the 25 studies reviewed by Zuin *et al.* that assessed the association between BAC and cardiovascular disease, coronary artery disease, intracranial artery disease, coronary artery calcification, and cervical and peripheral artery disease. The results of these studies confirmed that a statistically significant relationship exists between arterial calcification and other diseases, and the associated mortality can be analyzed. Therefore, the aforementioned authors concluded that mammography can be used as a screening tool for cardiovascular and coronary artery disease.

Polonsky and Greenland [15] described some observational studies that have demonstrated the presence of BAC acting as pivotal precursors of cardiovascular risk. However, the appearance of BAC does not clearly indicate the risk of increased cardiovascular disease. It may only represent long-term exposure to known cardiovascular risk factors. BAC has also been proven to be an indicator of calcification in other vascular beds. Calcification increases the stiffness of blood vessels and may explain that in addition to coronary artery disease and stroke, BAC is related to heart failure.

2.2 Introduction to RL

The most important characteristic of RL is learning from interaction. By definition, an RL agent must interact with its environment. According to the rewards or punishments obtained, the continuous learning of knowledge makes the RL agent more adaptable to the environment. The operation of RL is remarkably similar to the process by which humans learn knowledge. Therefore, RL is regarded as a vital general artificial intelligence approach. The formal definition of RL is that two objects exist and can interact; (1) Agents can sense the state of the external environment and rewards of the feedback, can learn, and can make decisions. The decision-making function of the agent refers to making different actions according to the state of the external environment, and the learning function refers to adjusting the strategy according to the rewards of the external environment; (2) The environment refers to all things outside the agent. The state of the agent is changed by the actions of the agent. The corresponding reward is fed back to the agent.

The four basic elements in RL (a , s , r , and p) are illustrated in Fig. 2; (1) The state s describes the environment, which can be discrete or continuous, and its state space is S ; (2) The action a describes the agent's behavior, which can be discrete or continuous, and its action space is A ; (3) Strategy $\pi(a|s)$ is a function with which the agent decides the next action a according to the environmental state s ; (4) The probability of the state transition $p(s_{t+1}|s_t, a_t)$ is the probability that the environment will change to the state s_{t+1} at the next moment after the agent makes an action according to the current state s_t , where t is the current time and $t + 1$ is the time of the next moment; (5) The instant reward $r(s, a, s')$ is a quantified function. After the agent makes an action a according to the current state s , the environment will feedback a reward to the agent. This reward is often related to the next moment state s' (or s_{t+1}) [2].

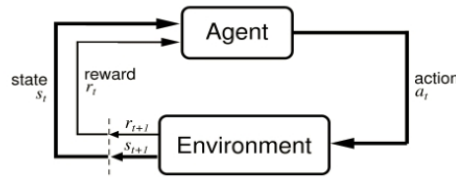


Fig. 2. Four basic elements of RL [17].

The strategy of a policy agent refers to how the agent decides the next action a according to the environmental state s . Policies can usually be divided into two groups: deterministic and stochastic policies. The deterministic policy involves mapping the function $\pi: S \rightarrow A$ from the state space to the action space. The random strategy involves determining the probability distribution of an agent selecting a certain action in a given environmental state. This probability distribution is defined as follows:

$$\pi(a|s) \triangleq p(a|s), \quad (1)$$

$$\sum_{a \in A} \pi(a|s) = 1. \quad (2)$$

In general, RL involves using a random strategy. Random strategies can have many advantages. For example, when learning, we can explore the environment better by introducing certain randomness. Taking the Markov decision process as an example, the agent starts from the sensed initial environment s_0 and then decides to make a corresponding action a_0 . The environment changes accordingly to the new state s_1 and feeds back an instant reward r_1 to the agent. Then, the agent performs an action a_1 according to state s_1 ; the environment changes to s_2 ; and the environment feeds back reward r_2 . This interaction can continue until s_n ends.

$$s_0, a_0, r_1, s_1, a_1, r_2, \dots, s_{t-1}, a_{t-1}, r_t, s_t, \dots, s_{n-1}, a_{n-1}, r_n, s_n \quad (3)$$

where $r_t = r(s_{t-1}, a_{t-1}, s_t)$ is the instant reward at time t . The process of the interaction between the agent and the environment can be regarded as a Markov decision process. This process has the following Markov random variable sequence: $s_0, s_1, \dots, s_t \in S$. The state s_{t+1} at the next moment only depends on the current state s_t . Thus, the following equation is obtained: $p(s_{t+1}|s_t, \dots, s_0) = p(s_{t+1}|s_t)$, where $p(s_{t+1}|s_t)$ is called the state transition probability.

$$\sum_{s_{t+1} \in \mathcal{S}} p(s_{t+1} | s_t) = 1 \tag{4}$$

In the Markov decision process, an additional variable action a is added. Thus, the state s_{t+1} at the next moment is related to the state s_t and action a_t at the current moment. Consequently, the following equation is obtained: $p(s_{t+1}|s_t, a_t, \dots, s_0, a_0) = p(s_{t+1}|s_t, a_t)$, where $p(s_{t+1}|s_t, a_t)$ is the probability of state transition. Given the strategy $\pi(a|s)$, the trajectory of the Markov decision process is $\tau = s_0, a_0, r_1, s_1, a_1, r_2, \dots, s_{T-1}, a_{T-1}, s_T, r_T$. The probability is given as follows:

$$p(\tau) = p(s_0, a_0, s_1, a_1, \dots, s_{T-1}, a_{T-1}) = p(s_0) \prod_{t=0}^{T-1} \pi(a_t | s_t) p(s_{t+1} | s_t, a_t). \tag{5}$$

Given the strategy $\pi(a|s)$, the cumulative reward received by the trajectory τ of an interaction between the agent and the environment is the total return, which is defined as follows:

$$G(\tau) = \sum_{t=0}^{T-1} r_{t+1} = \sum_{t=0}^{T-1} r(s_t, a_t, s_{t+1}). \tag{6}$$

Assuming that the environment has one or more special termination states, when the termination state is reached, the interaction process between an agent and the environment ends. This interactive process is called an episode or trial. If no termination state occurs in the environment, that is, if $T = 1$, the task is called a continuous RL task. The total return of a continuous RL task may be infinite. To solve this problem, a discount rate can be introduced for reducing the weight of forward returns. The discounted return is defined as follows:

$$G(\tau) = \sum_{t=0}^{T-1} \gamma^t r_{t+1} \tag{7}$$

where $\gamma \in [0, 1]$ is the discount rate. When the discount rate is close to 0, the agent cares more about the short-term return. When the discount rate is close to 1, the long-term return becomes more critical. In addition, because the strategy and state transition have some randomness, the trajectory obtained in each test is a random sequence and the total rewards obtained in each test are different. The goal of RL is to learn a strategy $\pi_\theta(a|s)$ to maximize the expected return, that is, the agent is expected to perform a series of actions to obtain as much average return as possible. The objective function of RL is defined as follows:

$$J(\theta) = E_{\tau \sim p_\theta(\tau)} [G(\tau)] = E_{\tau \sim p_\theta(\tau)} [\sum_{t=0}^{T-1} \gamma^t r_{t+1}] \tag{8}$$

where θ is the parameter of the strategy function. Thus, we should adjust the parameters to increase the probability of strategy $\pi(a|s)$ [18]. The objective function can be applied for the construction of deep RL models, such as the DQN and SARSA learning algorithms.

2.3 Application of Deep RL for Medical Image Processing

Deep RL has been used in applications of medical image processing, such as com-

puted tomography (CT) and magnetic resonance imaging (MRI). For example, Ali *et al.* [19] developed and validated an RL model based on a deep artificial neural network for the early detection of lung nodules in CT images of the chest. The aforementioned model is inspired by the AlphaGo system. It uses the original CT image as an input, treats the image as a set of states, and outputs the classification results regarding whether the image has nodules. The data used to train the aforementioned model was the lung nodule analysis challenge data obtained from the LIDC/IDRI database. The training data comprised 888 CT images with at least three-fourth agreement among the annotations of different radiologists. Of these 888 images, 590 had one or more nodules and 298 only had a single nodule. The experimental results indicated that the overall accuracy of the training results was 99.1%. Moreover, the sensitivity, specificity, positive predictive value, and negative predictive value of the training results were 99.2%, 99.1%, 99.1%, and 99.2%, respectively. However, the overall accuracy of the test results was 64.4%. Moreover, the sensitivity, specificity, positive predictive value, and negative predictive value of the test results were 58.9%, 55.3%, 54.2%, and 60.0%, respectively. Thus, the aforementioned system still has room for improvement.

Maicas *et al.* [20] proposed the automatic detection of breast lesions through the deep RL of dynamic contrast-enhanced MRI (DCE-MRI) images. This method was compared with the exhaustive search method. The aforementioned authors used an attention mechanism to accelerate the search of lesions in appropriate areas. This mechanism learns a search policy by training an artificial agent and then utilizes the search strategy during inference. Specifically, the aforementioned authors extended the DQN method to detect lesions with significant changes in shape, appearance, location, and size. A total of 117 DCE-MRI datasets were used in the experimental design analysis. The results indicated that the running time of lesion detection was considerably short, and the accuracy was maintained at approximately 80%.

Shen *et al.* [21] used deep RL methods to train and automatically adjust the system parameters. This approach caused the system to behave like a human. In the study of Shen *et al.*, pixel-based total variation rule items were used to optimize and reconstruct CT images repeatedly. Moreover, a parameter-tuning policy network (PTPN) was set up. This network was used to map the CT image patch to the output position of the specified direction and amplitude by adjusting the parameters of the patch center. End-to-end RL was used to train the PTPN. The results of the trained PTPN achieved similar or higher quality compared with the manually reconstructed CT image.

Ghesu *et al.* [7] followed a new paradigm to redesign the detection problem as an artificial agent for behavioral learning tasks. They used the capabilities of deep RL and multiscale image analysis to combine the anatomical appearance and object search models in a behavioral framework. The training object of an artificial agent must not only distinguish the target anatomical object from other parts of the body but also train how to discover the object through learning and follow the optimal navigation path of the target object in the imaging volume space. The aforementioned authors evaluated 1487 3D CT volume data samples from 532 patients, and the number of image slices was more than 500,000. The results proved that several anatomical structures were detected from a clinical acceptance perspective. The system developed by the aforementioned authors is superior to the most advanced technology (20% to 30% higher detection accuracy). The detection speed of the system developed by Ghesu *et al.* [7] was 2-3 times higher than that of

the other compared systems. Their system achieved unparalleled instant performance for large 3D CT scans.

Mahmud *et al.* [22] comprehensively reviewed of the use of deep RL techniques for exploring biological data. In addition, they applied deep learning techniques to different datasets and application fields and compared their performance. Finally, the aforementioned authors resolved research challenges and discussed future developments.

3. RESEARCH METHODS

The flowchart of applying a region growth algorithm and deep RL for the detection of BAC in mammograms is illustrated in Fig. 3. The entire research process involves the following steps: (1) image preprocessing, including removing the pectoral muscle area and reducing image noise by using a Gaussian blur filter; (2) image segmentation by experts for ROI annotation and use of the line-strength method and region growth algorithm; (3) deep RL by combining a CNN model and deep Q-learning; and (4) performance evaluation by computing the Intersection over Union (IoU). The following sections describe the image preprocessing, image segmentation, deep RL, and performance evaluation steps.

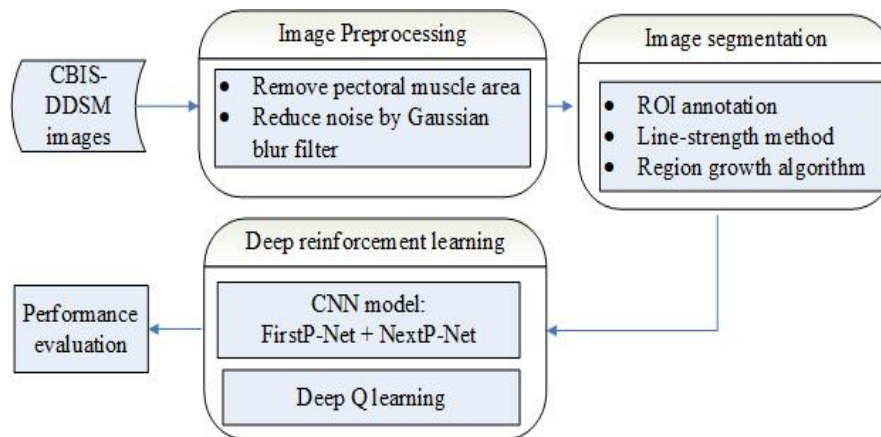


Fig. 3. Research flowchart.

3.1 Image Preprocessing

The diagnosis of BAC involves determining whether the two parallel calcified blood vessels on the mammogram can be easily identified. These easily identifiable parallel structures are called tram-like calcifications. Fig. 4 (a) illustrates a mammogram with BAC (green arrows), which can be defined as a typical arterial configuration of any visible linear calcium deposits that are different from the breast ducts along the periphery of the conical structure and have a length of at least 1 mm (Figs. 4 (b) and (c)). Fig. 5 is an example ROI of BAC arteries segmented from a mammogram. The length is defined as the longest continuous calcification segment. For example, in the arterial vessel AB depicted in the figure, the longest segment is CD.

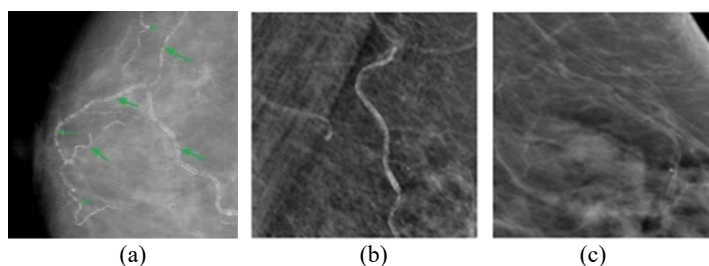


Fig. 4. Mammograms with BAC [23] and typical BAC artery configuration [24].

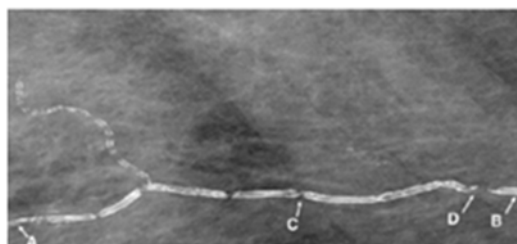


Fig. 5. Example of an ROI of the segmented BAC artery [25].

A mammogram is usually accompanied by an image label. Due to the high density of the label, X-rays cannot easily penetrate. In X-ray imaging, when useless high-brightness white color patches interfere with the subsequent image segmentation of the BAC, they must be removed during the preprocessing. The image tag removal process is illustrated in Fig. 6. Fig. 6 (a) displays an original mammogram. Fig. 6 (b) illustrates the binary image of Fig. 6 (a). Fig. 6 (c) is the color block with the largest area (*i.e.* breast). Fig. 6 (d) illustrates that image label and other noise outside the breast area are completely removed. This study used the method of marking color patches to remove useless image tags. First, the original X-ray image was binarized. After the binarization, only two levels of black and white remained. Similar pixels were merged to form a color block. A function defined by MATLAB was used to mark each color patch, record its area, locate the color patch with the largest area (*i.e.*, breast), and remove the remaining color patches (other noise outside the breast area) for completely removing the image tag and other noise outside the breast area.

During the mammography examination, a part of the pectoral muscle area connected to the breast tissue must be photographed from the mediolateral oblique perspective. Because of the high density of muscle tissue in this area, X-rays cannot easily penetrate it. Fig. 7 (a) indicates that the pectoral muscles are connected to the breast tissue in the X-ray image; thus, the pectoral muscle area cannot be removed in the same manner as the image label. This study used the method of threshold detection to remove the aforementioned area. Because the pectoral muscle area belongs to a high-brightness white color block, the gradation distribution between the pectoral muscle area and breast tissue can be found by observing the peak of the gradation in the histogram. Then, after the threshold has been found and the image has been binarized, the pectoral muscle and breast tissue can be separated. The histogram of the displayed image is illustrated in Fig. 7 (b). Fig. 7 (c) depicts

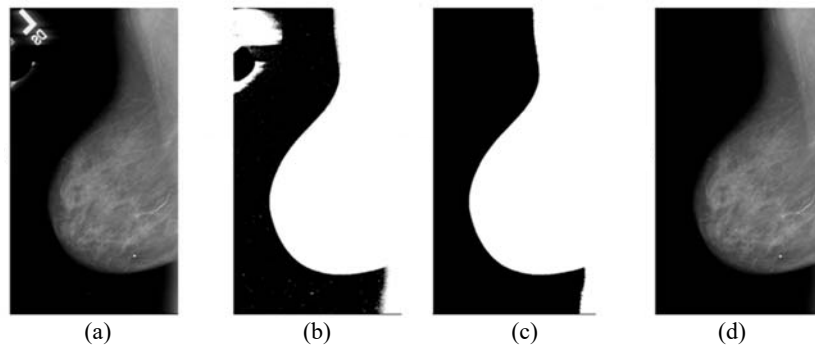


Fig. 6. Image label removal: (a) original mammogram; (b) binary image; (c) color block with the largest area; and (d) image after preprocessing.

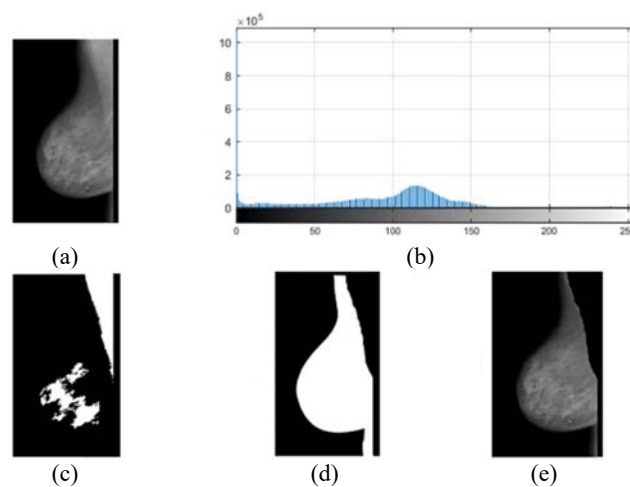


Fig. 7. Pectoral muscle area removal: (a) original mammogram; (b) histogram; (c) binary image; (d) image with reserved breast area; and (e) image after removing the pectoral muscle area.

the threshold binarized image. Fig. 7 (d) illustrates the reserved breast area. Fig. 7 (e) displays the mammogram obtained after removing the pectoral muscle area.

Typical original breast mammogram samples have different sizes. To facilitate the subsequent research, each mammogram was cropped to a size of 4000×2100 pixels. A mammogram is a grayscale image, and each pixel has 256 levels of intensity. Because the human breast has many tissues with similar gradations stacked on each other in X-ray images, suspicious areas with BAC are often difficult to identify. To reduce image noise and the level of detail of normal tissue, this study used Gaussian blur to make the outlines of suspicious areas more obvious.

To highlight the linear features of BAC and facilitate the subsequent image segmentation, this study used the line-strength algorithm proposed by Zwiggelaar *et al.* [26]. This algorithm can perform special image processing for mammograms after Gaussian blur filtering. The calculation formula of the line-strength algorithm for segmentation is defined as follows:

$$S = \alpha(L - N) + (1 - \alpha)(I - \alpha) \quad (9)$$

where S is the intensity value of the line segment, L is the average value of the gradation intensity of the pixels on the line segment, N is the average gradation intensity of the pixels in the square area through which the line segment passes, I is the original tone intensity, and G is the tone intensity after Gaussian filtering. The value of σ in Eq. (13) determines the size of the square area where N is calculated, and α is a parameter between 0 and 1. As per the study of Nava *et al.* [27], this study set α as 0.1.

3.2 Image Segmentation

The purpose of image segmentation is the automatic depiction, instead of the manual depiction, of the skeleton of the linear structure. Therefore, the goal of this study was to detect pixels that may represent more severe calcifications to persuade patients to control their cardiovascular disease risk factors. The entire image segmentation process is mainly divided into the following three stages.

3.2.1 Binarized image

For image binarization, this study input the result S of the line-strength algorithm as a threshold into a binarization function that compared each pixel with a given threshold to extract the linear structure with the highest image intensity. Pixels with higher image intensity are more likely to be calcified vessels.

3.2.2 Region growth algorithm

This study then used the region growth method to segment the binarized image further. The entire segmentation process mainly involved image area division, region growing, and image joining; (1) Image area division: Even after cropping, the area of the entire binarized image was still too wide. To facilitate regional growth, this study referred to the approach of Mazidi *et al.* [28] and divided the 4000×2100 -pixel binary image into six 2000×700 -pixel areas; (2) Region growing: The area with BAC was selected from the six areas, and the region growing method was used to perform segmentation. The region growth algorithm involves collecting pixels with similar gradation intensity to form a region. Specifically, a "seed" is first found in each region that must be divided as the starting point of the region growth. Then, the pixels in the adjacent area are continually examined to determine whether their gradation intensity is similar the pixels at the starting point. Pixels are added to an area until no more pixels meet the conditions for being added to the area. In this study, the seed point was set to a pixel with a gradation intensity of 255, and the condition for stopping the growth of the region was a critical value of 55; (3) Image joining: After the segmentation was completed, the six 2000×700 -pixel areas that were originally divided were joined to form the original image with a size of 4000×2100 pixels, which is the final segmentation resolution.

3.2.3 Performance evaluation

The performance evaluation of ROI extraction involved examining the performance of segmentation of the BAC area from the original mammogram by using the region

growth algorithm. The criterion of evaluation was the IoU, which is defined as follows:

$$IoU = \frac{GT \cap SR}{GT \cup SR} \tag{10}$$

where GT represents the ground truth, which is the area with BAC in the original mammo-gram, and SR represents the segmentation result, which is obtained using the region growth method. The detection and evaluation functions mainly focus on observing the intersection of the segmented image area and ground truth as a percentage of their joint area; thus, these functions evaluate the accuracy of image segmentation. The higher the percentage, the higher is the accuracy.

3.3 Deep RL Model

The structure of the deep RL network used for the target area segmentation of gray-scale images is illustrated in Fig. 8. The entire network architecture is mainly divided into two parts: FirstP-Net and NextP-Net. The FirstP-Net CNN is responsible for finding the first coordinate at the edge of the target area. The NextP-Net DQN must locate the coordinates of the next edge point according to the previous edge points and image information. The model must gradually obtain the segmentation result of a closed area by gradually finding the edge point to segment the target area. The architecture of FirstP-Net is illustrated in Fig. 9. It comprises an image input layer, followed by a convolutional layer that contains a convolution sublayer and a pooling sublayer, several residual learning modules (resblk), a concatenation layer, and a probability map of the target area. The output of FirstP-Net is the first coordinate at the edge of the target area.

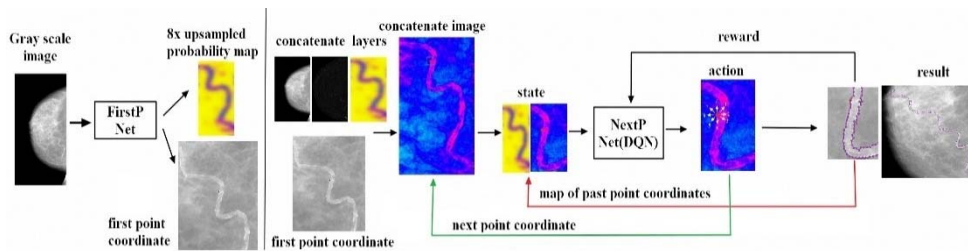


Fig. 8. Structure of the deep RL network used to process grayscale images.

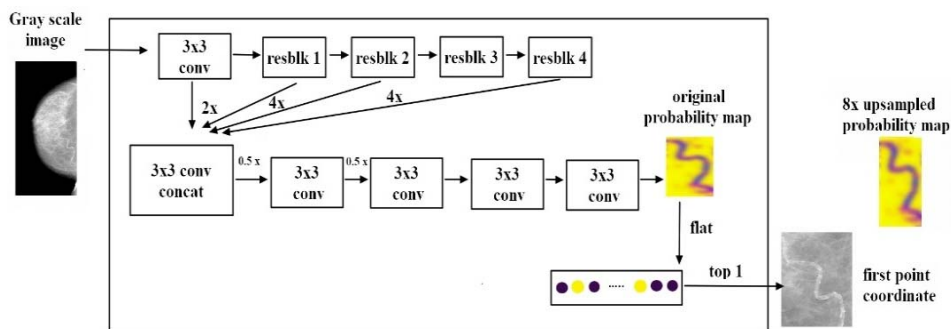


Fig. 9. Architecture of FirstP-Net.

The concatenation layer is responsible for creating the environment that interacts with the agents in the DQN. This layer generates four images: a grayscale image, a Sobel edge image, a probability map of the target area, and an image with all the previous edge points. The images generated by the concatenation layer are illustrated in Fig. 10.

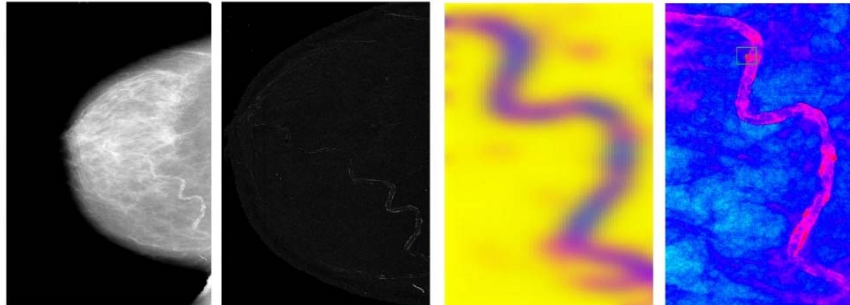


Fig. 10. Images generated by the concatenation layer.

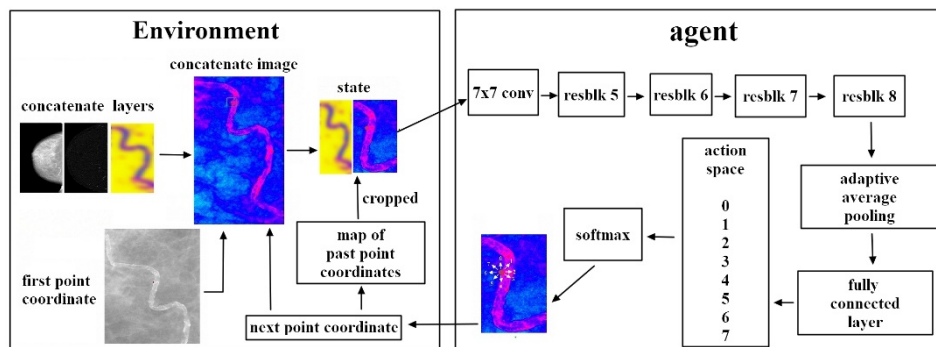


Fig. 11. Architecture of NextP-Net.

The architecture of the NextP-Net DQN is illustrated in Fig. 11. The fully connected layer must classify the actions that the agent can take, and the agent must select one of the possible actions. Seven choices exist for the agent's walking path. When the agent makes a choice, it becomes an immediate state input to the environment. Subsequently, the environment outputs the agent's new state and reward to the agent.

Reward is a type of feedback mechanism through which one can measure whether the agent's displays successful or failed behavior in the state. The agent must strengthen its behavior in a relatively positive or negative manner depending on the rewards received. Three types of rewards exist for DQNs in this research: difference IoU, edge distance, and point clustering. The preset IoU value was 0.5. When the ratio of the segmented area to the ground truth area was greater than 0.5, the agent received a high reward. The preset condition of the edge distance was that it must be less than 10 to obtain a reward. The closer the selected edge point was to the edge of the ground truth area, the higher was the accuracy. When the edge point selected during the segmentation process did not fall on the edge of

the ground truth area, it indicated that the edge of the target area was not accurately predicted. In this case, the obtained reward was negative and had a punitive effect. The purpose of the reward is to allow the selected edge point to be as close as possible to the edge of the ground truth area.

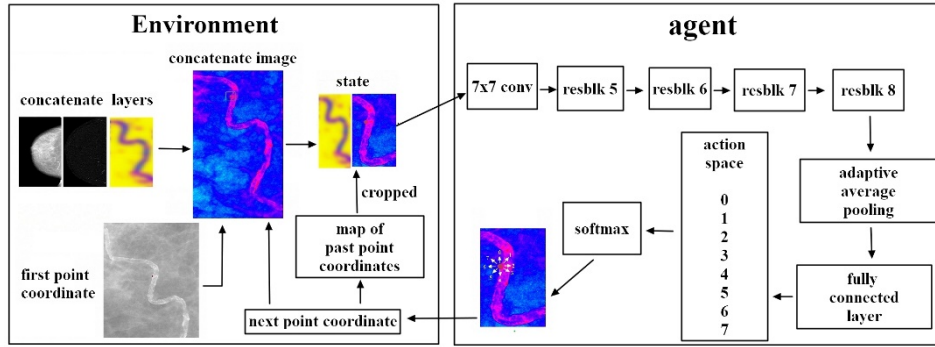


Fig. 11. Architecture of NextP-Net.

3.4 Performance Evaluation

The criteria used in this study to evaluate the performance of the deep RL network model were the precision, recall, and F -measure. Precision is a measure of the proportion of all predicted positive samples that are correctly classified as true positives. Recall is the proportion of all positive samples that are correctly classified as true positives. F -measure is the harmonious average of the precision and recall rate. These criteria can be obtained from the confusion matrix of the classification results in Table 1.

Table 1. Confusion matrix.

predicted class	actual class	
	positive	negative
positive	True Positives (TP)	False Positives (FP)
negative	False Negatives (FN)	True Negatives (TN)

$$Precision = \frac{TP}{TP + FP} \quad (11)$$

$$Recall = \frac{TP}{TP + FN} \quad (12)$$

$$F - measure = \frac{2 \times Precision \times Recall}{Precision + Recall} \quad (13)$$

4. EXPERIMENTAL DESIGN AND ANALYSIS

This section introduces the database and experimental environment as well as describes the segmentation results of the region growth algorithm and deep RL network.

4.1 Database

The mammograms used in this research were obtained from the Curated Breast Imaging Subset of the DDSM, which is an improved and updated version of the DDSM created by Lee *et al.* [29]. The images from this database were decompressed and converted to the DICOM format. Because BAC is typically classified as a benign case by physicians, this study selected 170 images from the benign dataset of the aforementioned database. Of the selected images, 50 were used to study the performance of the region growth algorithm and deep RL network. The 50 ground truth BAC samples used in this study had been annotated manually by experts.

4.2 Experimental Environment

The experiments in this study were performed on a laptop with a high-end graphics card. The laptop comprised an Intel Core i5-4200H octa-core processor, 8 GB of DDR3 2400 MHz RAM, and an NVIDIA GeForce GTX 820 GDDR5 8 GB GPU. The programming languages used were MATLAB and Python 3.6.4. Python, which includes pandas, numpy, matplotlib, git, scikit-learn, opencv-python 4.1.0.25, scikit-image 0.14.3, Shapely 1.6.4, post2, ciffi, scipy, and other library packages, runs on the Anaconda suite version of Jupyter Notebook. The deep RL network adopted in this study uses TensorFlow, PyTorch 0.4.0, and torchvision 0.2.1. Each input image segmented with the region growth algorithm must be divided into one or several BAC ROIs. Subsequently, the deep RL method must be executed. In addition, to increase the processing speed of the CNN, batch processing can be used in convolution operations.

4.3 Results of Segmentation with the Region Growth Algorithm

The main difference between the original mammogram and line-strength image was that the area of the ground truth had to be larger than the calcified blood vessels after line-strength algorithm processing. The reason for this criterion is that the main purpose of the line-strength method is to strengthen the identification of blood vessels with severe calcification. Fig. 12 presents a comparison of the process of recognizing calcified blood vessels from the original mammogram and from the image obtained after using the region growth algorithm. Fig. 12 (a) displays the mammogram obtained after Gaussian filtering. The line structure at the red arrow is the BAC. Fig. 12 (b) illustrates the result of image processing.

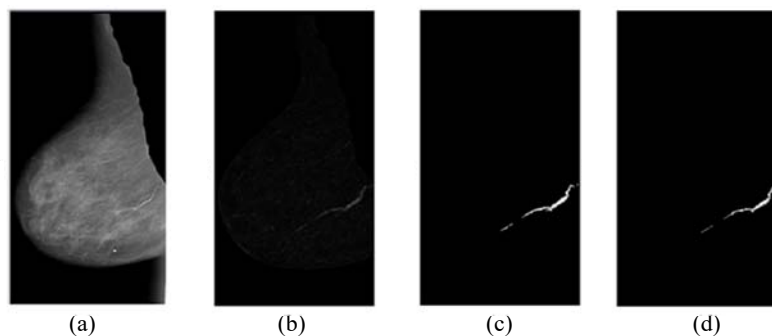


Fig. 12. Line-strength image: (a) Mammogram obtained after Gaussian filter filtering; (b) Image obtained after using the line-strength method; (c) Binary image; and (d) Image obtained after region growth algorithm processing.

The area indicated by the red arrow is the line-strength structure. Fig. 12 (c) depicts the binarized image obtained by inputting the binarization function with the result of the line-strength calculation ($S = 0.1113$) of the images. Fig. 12 (d) illustrates the image obtained after region growth algorithm processing. This image proves that most of the calcified blood vessels were detected. Fig. 13 illustrates a binary image divided into six regions before executing the region growth algorithm. Only regions containing calcified blood vessels were selected for region growth.

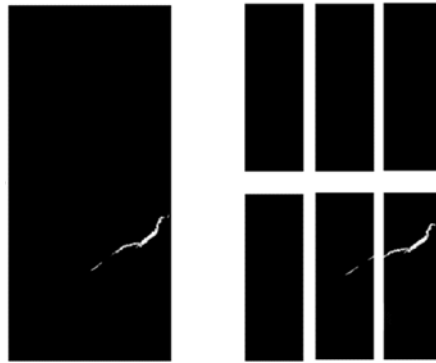


Fig. 13. Area division: (a) Binary image with BAC and (b) Image divided into six areas.

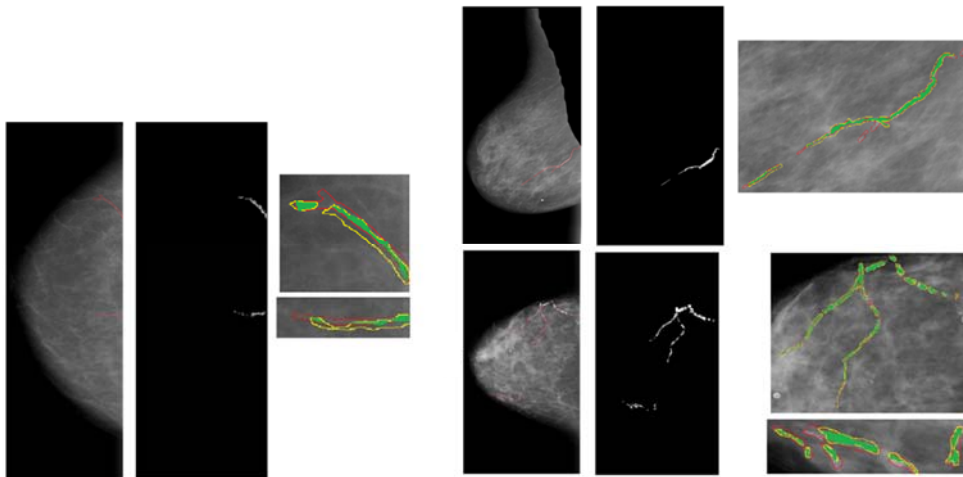


Fig. 14. Distribution of the union area and intersection area of three samples.

Fig. 14 illustrates the distribution of the joint area and intersection area. The area marked in red is the ground truth; the area marked in yellow line is the result of region growing; and the area marked in green is the intersection of the ground truth and region growing result. Fig. 14 (a) displays a sample with an IoU value of 0.56. Fig. 14 (b) depicts a sample with an IoU value of 0.75. Fig. 14 (c) illustrates a sample with an IoU value of 0.89. The average IoU of 50 samples was 0.7578, the minimum IoU value was 0.56, the maximum IoU value was 0.89, the median IoU value was 0.7539, the standard deviation was 0.0763, and the unit was mm^2 (for the region growth model).

4.4 Results of Segmentation with the Deep RL Network

The architecture and parameters of FirstP-Net and NextP-Net are listed in Tables 2 and 3, respectively. Deep RL fixes the input size of the image to 368×368 pixels. To train and test the proposed deep RL network, 290 images were used and randomly divided. A total of 70% of the images formed the training set, and 30% of the images formed the testing set.

Table 2. Architecture and parameters of FirstP-Net.

Type	Kernel	# of channels	Stride	Padding	Dilation	Output size
Conv-BN-ReLU	3×3	64	2	1	1	184×184×64
Maxpooling	3×3	64	2	1	1	92×92×64
Resblk 1	$\begin{bmatrix} 1 \times 1 & 64 \\ 3 \times 3 & 64 \\ 1 \times 1 & 256 \end{bmatrix} \times 2$	1	0	1	92×92×256	
		1	1	1		
		1	0	1		
Resblk 2	$\begin{bmatrix} 1 \times 1 & 128 \\ 3 \times 3 & 128 \\ 1 \times 1 & 512 \end{bmatrix} \times 2$	1	0	1	46×46×512	
		1	1	1		
		1	0	1		
Resblk 3	$\begin{bmatrix} 1 \times 1 & 256 \\ 3 \times 3 & 256 \\ 1 \times 1 & 1024 \end{bmatrix} \times 2$	1	0	1	46×46×1024	
		1	2	2		
		1	0	1		
Resblk 4	$\begin{bmatrix} 1 \times 1 & 512 \\ 3 \times 3 & 512 \\ 1 \times 1 & 2048 \end{bmatrix} \times 2$	1	0	1	46×46×2048	
		1	4	4		
		1	0	1		
Conv-BN-ReLU	3×3	64	1	1	1	184×184×64
Concat		256				184×184×256
Conv-BN	3×3	128	2	1	1	92×92×128
Conv-BN	3×3	128	2	1	1	46×46×128
Conv-BN	3×3	128	1	1	1	46×46×128
Conv	3×3	16	1	1	1	46×46×16
Conv	1×1	1	1	0	1	46×46×1

The experimental results of the deep RL network are illustrated in Fig. 15. The blue line represents the ground truth boundary, and the red point represents the first edge point found by FirstP-Net. The purple point is the walking path found by NextP-Net. Fig. 15 (a) displays an original mammogram. Fig. 15 (b) illustrates the image with ground truth. Fig. 15 (c) depicts the first edge point found by FirstP-Net. Fig. 15 (d) displays the points and walking path found by NextP-Net. Fig. 15 (e) presents the enlarged image of the area near the first edge point. To evaluate the segmentation performance of the deep RL network, we used 50 ground truth samples for testing. The average IoU of 50 samples was 0.8998, the minimum IoU value was 0.8533, the maximum IoU value was 0.9385, the median IoU was 0.9134, and the standard deviation of the IoU was 0.0241 (for the Deep RL 1 model).

Table 3. Architecture and parameters of NextP-Net.

Type	Kernel	# of channels	Stride	Padding	Dilation	Output size
Conv-BN-ReLU	7×7	64	2	3	1	26×26×64
Maxpooling	3×3	64	2	1	1	13×13×64
Resblk 5	$\begin{bmatrix} 3 \times 3 & 64 \\ 3 \times 3 & 64 \end{bmatrix} \times 1$		1	1	1	13×13×64
			1	1	1	
Resblk 6	$\begin{bmatrix} 3 \times 3 & 128 \\ 3 \times 3 & 128 \end{bmatrix} \times 1$		2	1	1	7×7×128
			1	1	1	
Resblk 7	$\begin{bmatrix} 3 \times 3 & 256 \\ 3 \times 3 & 256 \end{bmatrix} \times 1$		2	1	1	4×4×256
			1	1	1	
Resblk 8	$\begin{bmatrix} 3 \times 3 & 512 \\ 3 \times 3 & 512 \end{bmatrix} \times 1$		2	1	1	2×2×512
			1	1	1	
Average Global Pooling						1×1×512
FC						8

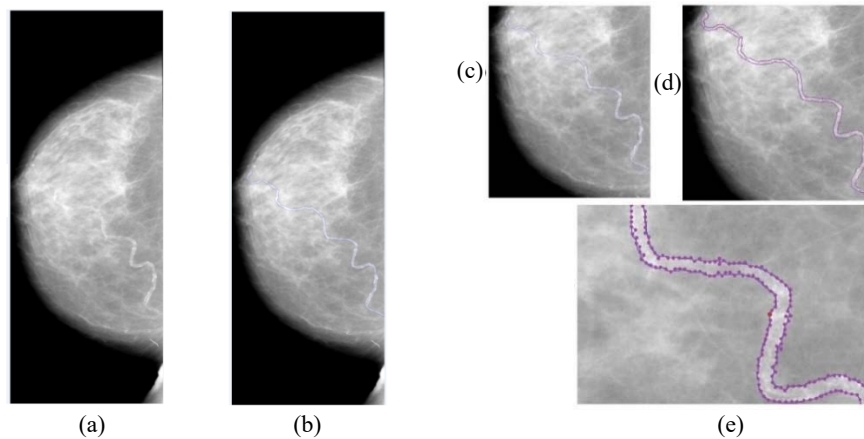


Fig. 15. (a) Original mammogram; (b) Ground truth; (c) First edge point; (d) Point and walking path; and (e) Enlarged image of the area near the first edge point.

The reward curve of NextP-Net is illustrated in Fig. 16. Fig. 16 (a) displays the curve of the difference IoU reward. Fig. 16 (b) illustrates the curve of the edge distance reward. Fig. 16 (c) depicts the curve of the point clustering reward. Fig. 16 (d) presents the curve of the total reward. The total reward is the sum of the aforementioned three rewards. The reward curves prove that the model continues the optimization process as the number of iterations increases to obtain rewards. The best performance was achieved in approximately 2000 iterations. At the end of the training, the reward values of the difference IoU, edge distance, and point clustering were 109.0760, 41.6081, and -2.4585 , respectively. Moreover, the total reward was 148.2256. The experimental results indicated that the precision, recall, and F -measure were 0.9157, 0.9273, and 0.9215, respectively.

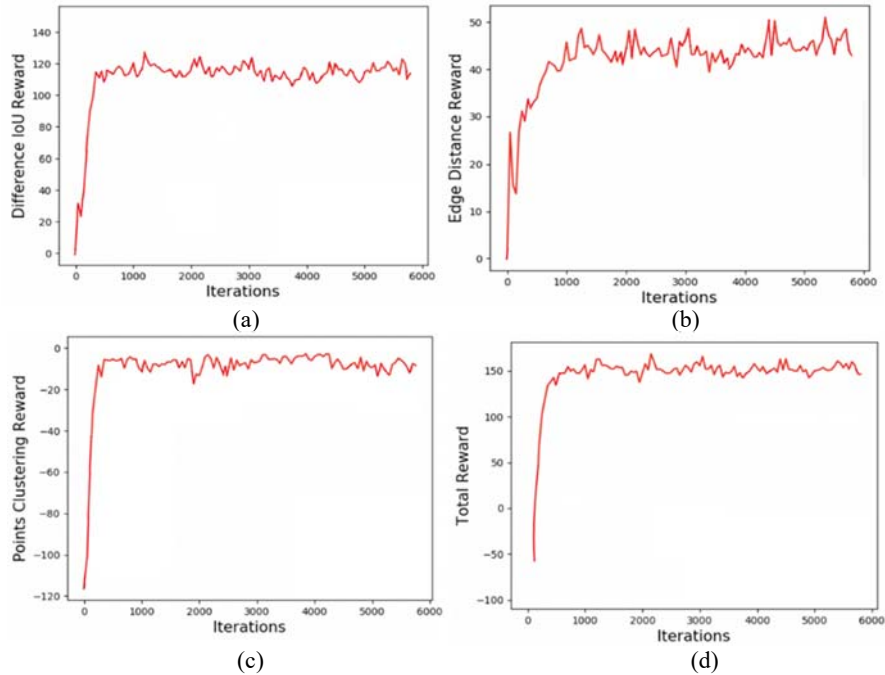


Fig. 16. Reward curve of NextP-Net: (a) Difference IoU reward; (b) Edge distance reward; (c) Points clustering reward; and (d) Total reward.

To improve the performance of deep RL for segmentation, we artificially augmented the 290 samples by using 90° , 180° , and 270° rotation transformations, vertically mirroring the transformed images, and then rotating them again. These actions produced 2320 (290×8) images from the original 290 images. We randomly assigned 70% of the images to a training set and 30% to a testing set. When the image files were sequenced by their name, the precision, recall, and F -measure were 0.9432, 0.9547, and 0.9489, respectively. In the aforementioned case, the average IoU of 50 samples was 0.9278, the minimum value IoU was 0.8975, the maximum IoU was 0.9549, the median IoU was 0.9283, and the standard deviation of the IoU was 0.0138 (Deep RL 2 model). When the image files were placed randomly by their name, the precision, recall, and F -measure were 0.9498, 0.9575, and 0.9536, respectively. In the aforementioned case, the average IoU of 50 samples was 0.9355, the minimum IoU value was 0.9010, the maximum IoU value was 0.9591, the median IoU was 0.9363, and the standard deviation of the IoU was 0.0132 (Deep RL 3 model).

The performance of the deep RL network is summarized in Table 4. The higher the number of samples, the better was the performance. To compare the performance of the region growth algorithm and deep RL network for BAC detection, Table 5 presents the IoU descriptive statistics of different segmentation methods. The analysis of variance (ANOVA) results listed in Table 6 indicate significant differences in the IoU among these four methods because the F -value was 204.807 and the P -value was 0.00, which is less than α at the 0.05 level. The multiple comparison results obtained through Scheffe post hoc testing indicate that among the four adopted models, only Deep RL 2 and Deep RL 3

had no significant difference. Table 7 lists the means for the groups in homogeneous subsets. The results in Table 7 prove that the Deep RL 2 and Deep RL 3 models outperformed the Deep RL 1 and region growth models.

Table 4. Performance of the deep RL network.

Methods	Samples	Precision	Recall	F-measure
Deep RL 1	290	.9157	.9273	.9215
Deep RL 2	2320	.9432	.9547	.9489
Deep RL 3	2320	.9498	.9575	.9536

Table 5. IoU descriptive statistics of different segmentation methods.

Methods	Samples	Mean	Std. Dev.	Minimum	Maximum
Region Growth	50	.7578	.0763	.56	.89
Deep RL 1	50	.8998	.0241	.85	.94
Deep RL 2	50	.9282	.0134	.90	.95
Deep RL 3	50	.9360	.0137	.90	.96
Total	200	.8805	.0830	.56	.96

Table 6. ANOVA results.

	Sum of Squares	df	Mean Square	F	Sig.
Between Groups	1.039	3	.346	204.807	.000
Within Groups	.331	196	.002		
Total	1.371	199			

Table 7. Means for groups in homogeneous subsets.

Method	N	Subset for alpha = 0.05		
		1	2	3
Region Growth	50	.7578		
Deep RL 1	50		.8998	
Deep RL 2	50			.9282
Deep RL 3	50			.9360
Sig.		1.000	1.000	.8260

4.4 Comparison Experiments

In order to test the performance of deep RL on BAC detection, we compared other four deep neural networks (DNN) including Cascade R-CNN, Grid R-CNN, YOLO, and RetinaNet. Cascade R-CNN is a multi-stage target detection architecture, which consists of a series of detectors trained with continuously increasing IoU thresholds, so that more choices can be made for the close false positive sequences [30]; Grid R-CNN uses a grid guided positioning mechanism for accurate object detection. Unlike traditional regression-based methods, Grid R-CNN clearly obtains spatial information and has the position-sensitive characteristics of a fully convolutional architecture [31]; YOLO integrates a complete convolutional neural network. The network is applied to the entire image, it divides the input image into grids, and predicts the bounding box and probability of each grid to detect the target [32]; RetinaNet is composed of a backbone network and two task-specific subnets. The backbone network is responsible for calculating the convolution fea-

ture map on the entire input image, and it is an unconventional convolution network [33]. The results of the DNN experiment are shown in Table 8, and Table 9 is IoU descriptive statistics of different DNN methods. The experimental results show that the Deep RL 3 model outperforms other DNN models.

Table 8. Comparison deep RL network with other DNN models.

Methods	Samples	Precision	Recall	F-measure	Accuracy
Cascade R-CNN	2320	.8971	.8868	.8919	89.22%
Grid R-CNN	2320	.8520	.8404	.8461	84.52%
YOLO v3	2320	.7980	.7842	.7910	79.04%
RetinaNet	2320	.8813	.8687	.8749	87.75%
Deep RL 3	2320	.9498	.9575	.9536	95.46%

Table 9. IoU descriptive statistics of different DNN methods.

Methods	Samples	Mean	Std. Dev.	Minimum	Maximum
Cascade R-CNN	50	.7519	.10128	.57	.89
Grid R-CNN	50	.6690	.12352	.52	.86
YOLO v3	50	.6195	.08681	.51	.84
RetinaNet	50	.6996	.04301	.55	.86
Deep RL 3	50	.9360	.0137	.90	.96

5. CONCLUSION

This study compared the performance of the region growth algorithm and deep RL network for identifying BAC in mammograms. The experimental results indicated that the deep RL network with numerous samples significantly outperformed the regional growth method. The best precision, recall, and F -measure of the deep RL network were 0.9498, 0.9575, and 0.9536, respectively. For the optimal RL network, the average IoU for 50 samples was 0.9355, the minimum IoU value was 0.9010, the maximum IoU value was 0.9591, the median IoU value was 0.9363, and the standard deviation of the IoU was 0.0132. The poor performance of the region growth method is related to the line-strength algorithm. The less obvious calcified blood vessels must be diluted after image processing, which affects the results of the region growing method. Therefore, the regional growth method is currently only suitable for the preliminary auxiliary judgment of BAC by a radiologist rather than as an independent diagnostic method. The experimental results of the deep RL network appear to be ideal; however, because only seven choices were available related to the agent's walking path, the walking path was prone to a 90° sharp turn or even a hairpin bend where the calcification was relatively light or the blood vessel was bent. The problem of including normal tissue in the calcified area or judging the calcified area as normal tissue must be solved.

In this study, obtaining image data was difficult and the hardware equipment performed inadequately. We recommend the establishment of a database that specifically collects mammograms of BAC. Such a database could facilitate follow-up research. In the future, we plan to use a portion of our research funding to upgrade our hardware equipment.

ACKNOWLEDGMENT

We are grateful to the Ministry of Science and Technology of Taiwan for providing the research grant that supported this work (MOST 108-2221-E-415-016-MY2) and acknowledge the 33rd IPPR Conference on Computer Vision, Graphics, and Image Processing, National Chiao Tung University, Hsinchu, Taiwan, August 16-18, 2020.

REFERENCES

1. Y. LeCun, Y. Bengio, and G. Hinton, "Deep learning," *Nature*, Vol. 7553, 2015, pp. 436-444.
2. X. P. Qiu, "Neural networks and deep learning," <https://nndl.github.io/>, 2019.
3. H. Mao, M. Alizadeh, I. Menache, and S. Kandula, "Resource management with deep reinforcement learning," in *Proceedings of the 15th ACM Workshop on Hot Topics in Networks*, 2016, pp. 50-56.
4. M. Zuin, G. Rigatelli, F. Scaranello, S. G. Ribecco, C. Picariello, and G. Zuliani *et al.*, "Breast arterial calcifications on mammography and coronary artery disease: A new screening tool for cardiovascular disease?" *International Journal of Cardiology*, Vol. 220, 2016, pp. 310-311.
5. N. Dhungel, G. Carneiro, and A. P. Bradley, "The automated learning of deep features for breast mass classification from mammograms," *Medical Image Computing and Computer-Assisted Intervention*, 2016, pp. 106-114.
6. J. C. Caicedo and S. Lazebnik, "Active object localization with deep reinforcement learning," in *Proceedings of IEEE International Conference on Computer Vision*, 2015, pp. 2488-2496.
7. F. C. Ghesu, B. Georgescu, Y. Zheng, S. Grbic, A. Maier, J. Hornegger, and D. Comaniciu, "Multiscale deep reinforcement learning for real-time 3D-landmark detection in CT scans," *IEEE Transactions on Pattern Analysis and Machine Intelligence*, Vol. 41, 2019, pp. 176-189.
8. G. A. Rummery and M. Niranjan, "On-line Q-learning using connectionist systems," Technical Report No. 166, Department of Engineering, University of Cambridge, 1994.
9. J. B. Travnik, K. W. Mathewson, R. S. Sutton, and P. M. Pilarski, "Reactive reinforcement learning in asynchronous environments," <https://www.frontiersin.org/articles/10.3389/frobt.2018.00079/full>, 2018.
10. M. A. Rotter, P. F. Schnatz, A. A. Currier Jr, and D. M. O'sullivan, "Breast arterial calcifications (BACs) found on screening mammography and their association with cardiovascular disease," *Menopause*, Vol. 15, 2008, pp. 276-281.
11. E. J. Hendriks, P. A. de Jong, Y. van der Graaf, W. P. Mali, Y. T. van der Schouw, and J. W. Beulens, "Breast arterial calcifications: a systematic review and meta-analysis of their determinants and their association with cardiovascular events," *Atherosclerosis*, Vol. 239, 2015, pp. 11-20.
12. E. J. Hendriks, J. W. Beulens, W. P. Mali, D. Beijerinck, Y. van der Graaf, P. A. de Jong, and Y. T. van der Schouw, "Breast arterial calcifications and their association with incident cardiovascular disease and diabetes," *Journal of the American College*

- of Cardiology*, Vol. 65, 2015, pp. 859-860.
13. T. Chadashvili, D. Litmanovich, F. Hall, and P. J. Slanetz, "Do breast arterial calcifications on mammography predict elevated risk of coronary artery disease?" *European Journal of Radiology*, Vol. 85, 2016, pp. 1121-1124.
 14. M. Zuin, G. Rigatelli, F. Scaranello, S. G. Ribecco, C. Picariello, and G. Zuliani, "Breast arterial calcifications on mammography and coronary artery disease: A new screening tool for cardiovascular disease?" *International Journal of Cardiology*, Vol. 220, 2016, pp. 310-311.
 15. T. S. Polonsky and P. Greenland, "Breast arterial calcification," *Circulation*, Vol. 135, 2017, pp. 499-501.
 16. J. Y. Yeh, S. Y. Wu, and S. W. Chan, "Deep reinforcement learning for breast arterial calcification detection on mammograms," in *Proceedings of the 33rd IPPR Conference on Computer Vision, Graphics, and Image Processing*, 2020, pp. 955-962.
 17. R. S. Sutton and A. G. Barto, *Reinforcement Learning: An Introduction*, The MIT Press, MA, 2011.
 18. X. Qiu, "Neural networks and deep learning," <https://mndl.github.io/>, 2020.
 19. I. Ali, G. R. Hart, G. Gunabushanam, Y. Liang, W. Muhammad, B. Nartowt, M. Kane, X. Ma, and J. Deng, "Lung nodule detection via deep reinforcement learning," *Frontiers in Oncology*, Vol. 8, 2018, pp. 1-7.
 20. G. Maicas, G. Carneiro, A. P. Bradley, J. C. Nascimento, and I. Reid, "Deep reinforcement learning for active breast lesion detection from dcmri," in *Proceedings of International Conference on Medical Image Computing and Computer-Assisted Intervention*, 2017, pp. 665-673.
 21. C. Shen, Y. Gonzalez, L. Chen, S. B. Jiang, and X. Jia, "Intelligent parameter tuning in optimization-based iterative CT reconstruction via deep reinforcement learning," *IEEE Transactions on Medical Imaging*, Vol. 37, 2018, pp. 1430-1439.
 22. M. Mahmud, M. S. Kaiser, A. Hussain, and S. Vassanelli, "Applications of deep learning and reinforcement learning to biological data," *IEEE Transactions on Neural Networks and Learning Systems*, Vol. 29, 2018, pp. 2063-2079.
 23. R. A. Akinola, O. A. Ogbera, J. A. Onakoya, C. E. Enabulele, and I. O. Fadeyibi, "Mammograms and breast arterial calcifications: looking beyond breast cancer: a preliminary report," *BMC Research Notes*, Vol. 207, 2011, pp. 1-6.
 24. M. H. Zgheib, S. S. Buchbinder, N. Abi Rafeh, M. Elya, C. Raia, and K. Ahern *et al.*, "Breast arterial calcifications on mammograms do not predict coronary heart disease at coronary angiography," *Radiology*, Vol. 254, 2010, pp. 367-373.
 25. J. Wang, H. Ding, F. A. Bidgoli, B. Zhou, C. Iribarren, S. Molloy, and P. Baldi, "Detecting cardiovascular disease from mammograms with deep learning," *IEEE Transactions on Medical Imaging*, Vol. 36, 2017, pp. 1172-1181.
 26. R. Zwiggelaar, S. M. Astley, R. M. Borris, and C. J. Taylor, "Linear structures in mammographic images: detection and classification," *IEEE Transactions on Medical Imaging*, Vol. 23, 2004, pp. 1077-1086.
 27. E. Nava, I. Barba, F. Sendra, and C. G. Rebollo, "Quantification of vascular calcifications on digitized mammograms," in *Proceedings of International Conference on Digital Mammography*, LNCS Vol. 6136, 2010, pp. 183-190.
 28. N. Mazidi, C. Roobottom, and G. Masala, "Automatic quantification of breast arterial calcification on mammographic images," *Innovation in Medicine and Healthcare Sys-*

- tems, and Multimedia*, Vol. 145, 2019, pp. 283-292.
29. R. S. Lee, F. Gimenez, A. Hoogi, K. K. Miyake, M. Gorovoy, and D. L. Rubin, "A curated mammography data set for use in computer-aided detection and diagnosis research," *Scientific Data*, Vol. 4, 2017, pp. 1-9.
 30. Z. Cai and N. Vasconcelos, "Cascade r-cnn: Delving into high quality object detection," in *Proceedings of IEEE Conference on Computer Vision and Pattern Recognition*, 2018, pp. 6154-6162.
 31. X. Lu, B. Li, Y. Yue, Q. Li, and J. Yan, "Grid r-cnn," in *Proceedings of IEEE Conference on Computer Vision and Pattern Recognition*, 2019, pp. 7363-7372.
 32. J. Redmon, S. Divvala, R. Girshick, and A. Farhadi, "You only look once: Unified, real-time object detection," in *Proceedings of IEEE Conference on Computer Vision and Pattern Recognition*, 2016, pp. 779-788.
 33. P. Goyal and H. Kaiming, "Focal loss for dense object detection," *IEEE Transactions on Pattern Analysis and Machine Intelligence*, Vol. 39, 2018, pp. 2999-3007.



Jinn-Yi Yeh (葉進儀) received the B.S. degree from Chung-Yuan Christian University, Taiwan, in 1987 and the M.S. and Ph.D. degrees from the University of Texas at Arlington in 1993 and 1997, respectively. He is presently a Professor in the Department of Management Information Systems, National Chiayi University, Taiwan. His research interests focus on data mining, medical image processing, and deep learning.



Sheng-You Wu (吳聲佑) received the B.S. degree in Department of Management Information Systems from Yuan Ze University, Taiwan. He is a graduate student in Department of Management Information Systems, National Chiayi University, Taiwan. His research interests include medical image processing and deep learning.



Siwa Chan (陳詩華) received the bachelor of Medicine from Kaohsiung Medical University, and M.S. of Health and Medical Engineering from Feng Chia University, Taiwan. She is presently a M.D. in Department of Medical Imaging, Taichung Tzu Chi Hospital, Taiwan.